

Mercury-Ar χ es: a high-performance n-body code for planet formation studies

Diego Turrini^{a,b}, Sergio Fonte^c, Romolo Politi^{b,c}, Danae Polychroni^{a,b}, Scigé J. Liu^c, Paolo Matteo Simonetti^{b,d}, Simona Pirani^e

^aINAF - Osservatorio Astrofisico di Torino, Strada Osservatorio 20, Pino Torinese, 10020, , Italy

^bICSC – National Research Centre for High Performance Computing, Big Data and Quantum Computing, Via Magnanelli 2, Casalecchio di Reno, 40033, , Italy

^cINAF - Istituto di Astrofisica e Planetologia Spaziali, Via Fosso del Cavaliere 100, Rome, 00133, , Italy

^dINAF - Osservatorio Astronomico di Trieste, Via G.B. Tiepolo 11, Trieste, 34143, , Italy

^eSharkmob, Malmö, Sweden

Abstract

Forming planetary systems are populated by large numbers of gravitationally interacting planetary bodies, spanning from massive giant planets to small planetesimals akin to present-day asteroids and comets. All these planetary bodies are embedded in the gaseous embrace of their native protoplanetary disks, and their interactions with the disk gas play a central role in shaping their dynamical evolution and the outcomes of planet formation. These factors make realistic planet formation simulations extremely computationally demanding, which in turn means that accurately modeling the formation of planetary systems requires the use of high-performance methods. The planet formation code MERCURY-Ar χ es was developed to address these challenges and, since its first implementation, has been used in multiple exoplanetary and Solar System studies. MERCURY-Ar χ es is a parallel n-body code that builds on the widely used MERCURY code and is capable of modeling the growth and migration of forming planets, the interactions between planetary bodies and the disk gas, as well as the evolving impact flux of planetesimals on forming planets across the different stages of their formation process. In this work we provide the up-to-date overview of its physical modeling capabilities and the first detailed description of its high-performance implementation based on the OpenMP directive-based parallelism for shared memory environments, to harness the multi-thread and vectorization features of modern processor architectures.

Keywords: Planet formation, Scientific Computing, Parallel Simulations, N-body Methods, Fortran, OpenMP

1. Introduction

The MERCURY n-body simulation code (Chambers, 1999) has been the tool of choice for planetary dynamics and terrestrial planet formation studies for decades, enabling more than 1600 investigations to date, and is still widely used in the planetary and exoplanetary science communities. Its open nature, intuitive structure, and clear programming style favored the branching of new versions, such as SMERCURY (Lissauer et al., 2012) for the study of spin-orbit interactions or MERCURY-T (Bolmont et al., 2015) for the study of tides, and the development of libraries implementing new modeling capabilities, like the symplectic mapping of binary systems (DPI, Turrini 2015; Nigoni et al. 2025 based on Chambers et al. 2002) and the Yarkovsky-O’Keefe-Radzievskii-Paddack effect (Fenucci and Novaković, 2022). MERCURY also serves as the n-body engine for the NGPPS planetary population synthesis model (Emsenhuber et al., 2021).

New n-body simulation packages have been developed by the community in recent years, introducing parallel or GPU-computing capabilities to allow for addressing more complex dynamical and collisional systems: REBOUND (Rein and Liu, 2012), GENGA (Grimm and Stadel, 2014) and GENGA II (Grimm et al., 2022), and GLISSE (Zhang and Gladman, 2022). No n-body current code, however, is optimized for the study of the earliest phases in the life of planetary systems, when forming planets and planetesimals are embedded into their native

protoplanetary disk and evolve together with it. In this work we present the first complete and self-contained description of the modeling and computational features Mercury-Ar χ es, an n-body planet formation code combining an high-performance implementation of the hybrid symplectic algorithm of the MERCURY code with a library allowing to model the main physical processes shaping the formation of planetary systems within their native protoplanetary disks.

The modeling features provided by MERCURY-Ar χ es allow for high-resolution explorations of the interactions between forming planets and the protoplanetary disks that surround them, and for the detailed characterization of how the planets alter the environment in which they are forming and how these alterations affect the planets themselves. The growth of massive planets is known to alter the dynamical equilibrium of the planetesimal disks embedded in the native circumstellar disks (Safronov, 1972; Weidenschilling et al., 1998; Turrini et al., 2011), causing the planetesimals to become dynamically excited and start intense collisional cascades (Weidenschilling et al., 2001; Turrini et al., 2012, 2019) long before the protoplanetary disks transition into debris disks. The dynamical excitation of the planetesimal disk results in its compositional remix and the transport of volatile elements across different disk regions (Safronov, 1972; Weidenschilling et al., 2001; Turrini and Svetsov, 2014; Turrini et al., 2015). This excitation process does not depend solely on planetary perturbations but is enhanced by disk gravity and countered by aerodynamic drag

(Weidenschilling, 1977; Ward, 1981; Nagasawa et al., 2000, 2019). Notwithstanding the critical role played by these processes in shaping the earliest phases in the life of planetary systems, they are still under-explored due to the computational challenges their modeling presents (e.g. Turrini et al., 2015, 2018, 2022; Feinstein et al., 2025, and references therein).

MERCURY- Δ RES has allowed for the first self-consistent studies of these processes in the circumstellar disks surrounding young stars (Turrini et al., 2019; Bernabò et al., 2022; Polychroni et al., 2025) and the Sun (Sirono and Turrini, 2025). The capability of resolving the concurrent effects of planetary perturbations, aerodynamic drag and disk gravity, while tracking the source regions of the planetesimals, recently allowed for quantifying the dynamical transport and implantation of primordial comets into the inner Solar System and the duration of their collisional cascade responsible for the formation of chondrules (Sirono and Turrini, 2025). In parallel, the possibility of characterizing the role of disk gravity as a function of the physical property of the disk allowed to explore how the intensity of the transport and remixing is affected by the observational uncertainty on the masses of protoplanetary disks and of their embedded planets (Polychroni et al., 2025).

The dynamical excitation of the planetesimals affects the very planets that stir the planetesimal disk (Turrini et al., 2015; Shibata and Ikoma, 2019; Shibata et al., 2020), enhancing the flux of impactors that hit the planets during their growth and migration. The detailed characterization of the dynamical state of the protoplanetary disk and of the temporal evolution of the physical and gravitational cross-sections of the growing planets of MERCURY- Δ RES allowed for the realistic quantification of the accretion of planetesimals by forming planets during the growth and migration across the native disks (Turrini et al., 2021, 2023; Polychroni et al., 2025). The record of their source regions allowed in turn to quantify the accretion efficiency across the different compositional regions of protoplanetary disk and the resulting composition of the young planets (Turrini et al., 2021; Pacetti et al., 2022; Fonte et al., 2023; Polychroni et al., 2025).

While the fundamental aspects of the modeling features of MERCURY- Δ RES were introduced in Turrini et al. (2019) and Turrini et al. (2021), no self-contained and updated description of its modeling algorithms is available in the literature. As an example, Turrini et al. (2019) adopted the gas drag treatment from Brasser et al. (2007), which was later found to implicitly hard-wire a number of fixed disk parameters into its numerical constants and to present possible discontinuities between the different drag regimes (Stoyanovskaya et al., 2020), resulting in its substitution with a more general implementation (see Sect. 3.1) after the study of Turrini et al. (2021). Similarly, while Turrini et al. (2019) and Turrini et al. (2021) reported that MERCURY- Δ RES was based on a parallel version of the hybrid symplectic algorithm of the MERCURY code, no details were provided on the adopted optimization and parallelization approach since they were beyond the scope of those studies.

In the following we fill these gaps by first describing MERCURY+, the parallel n-body engine of MERCURY- Δ RES (Sect. 2) and the updated multi-physics engine for planet formation studies (Sect. 3). Finally, we illustrate the performance and scal-

ability of MERCURY- Δ RES on realistic, non-idealized use cases based on previous investigations using both consumer-grade and cluster infrastructures (Sect. 4).

2. MERCURY+, the n-body engine of MERCURY- Δ RES

MERCURY+ builds on MERCURY 6 (Chambers, 1999) and provides an high-performance implementation of its hybrid symplectic integrator. This design choice is motivated by the desirable properties of this integration schemes for planet formation studies, since it combines the computational efficiency of symplectic algorithms with the capability of resolving close encounters and collisions among planetary bodies.

Symplectic algorithms (Wisdom and Holman, 1991; Kinoshita et al., 1991) are a family of leapfrog integration schemes that are about an order of magnitude faster than conventional n-body algorithms and allow to simulate the long-term evolution of planetary systems without undergoing secular accumulation of the energy error. To improve the accuracy and numerical stability of the Keplerian evolution of the planetary orbits, MERCURY- Δ RES interfaces with the WHFAST library of the REBOUND code (Rein and Tamayo, 2015) in place of MERCURY’s original subroutines for the computation of the Keplerian drift. The seamless interface between MERCURY (FORTRAN77) and WHFAST (C99) is guaranteed by a Fortran95 wrapper.

The energy conservation property of symplectic algorithms is guaranteed as long as the hierarchical structure of the dynamical system is preserved. For planetary systems this means that the dynamical evolution of the bodies is dominated by the gravitational field of the host star, a condition that is violated during close encounters between planetary bodies. During close encounters, Mercury’s hybrid symplectic algorithm switches to the high-precision non-symplectic Bulirsh–Stoer integration scheme to accurately reproduce the dynamical evolution of the involved bodies while their gravitational interactions are comparable in magnitude to the gravitational pull of the star (Chambers, 1999).

2.1. High-performance features of the n-body engine

The hybrid symplectic scheme of MERCURY+ has been parallelized and vectorized with OpenMP to take advantage of the SIMD (single instruction, multiple data) capabilities of modern multi-core architectures. The HPC implementation of MERCURY+ is based on the following design philosophy:

- we preserved the original structure of MERCURY and adopted solutions that maximize the interoperability with legacy codes and libraries designed to work with it, to facilitate their integration with MERCURY+. This choice led to the adoption of the directive-based OpenMP model for the porting to HPC;
- we focused the development on value-safe parallelization solutions to enforce reproducibility between the parallel and serial versions of the code. This design choice has been adopted to facilitate the debugging and validation of existing and future parallel sections of the code;

- we explicitly instructed the compiler to combine parallelization and vectorization whenever possible to provide consistent performances across different compilers. Analogously, we implemented documented bug fixes to minimize the dependencies on runtime environments and provide the users with a robust and flexible n-body integrator;

We provide details on the implementation of this design philosophy in the following sections. The list of parallel subroutines within **MERCURY+** is the following: `MCE_BOX`, `MCE_HILL`, `MCE_SNIF`, `MCO_B2H`, `MCO_DH2H`, `MCO_H2B`, `MCO_H2DH`, `MCO_IDEN`, `MDT_BS1`, `MDT_BS2`, `MDT_HY`, `MFO_DRCT`, `MFO_USR`, `MFO_HY`, `MFO_HKCE`. The selection of the subroutines to parallelize was based on the cumulative profiling outputs obtained through **GPROF** across all science cases where we took advantage of **MERCURY-AR χ ES** (Turrini et al., 2019, 2021, 2023; Bernabò et al., 2022; Polychroni et al., 2025; Sirono and Turrini, 2025).

From a technical point of view the subroutine `MDT_BS1`, implementing the general case of the Bulirsh-Stoer integrator in **MERCURY**, is not used directly by **MERCURY-AR χ ES** as the hybrid symplectic integrator makes use of `MDT_BS2`, an implementation of the Bulirsh-Stoer integrator specific for the use of conservative forces. However, since `MDT_BS1` and `MDT_BS2` share a common structure, we parallelized both for future use. In the following, we provide illustrative examples of the optimizations introduced in **MERCURY+**, while Sect. 4 will showcase typical use cases and workloads of **MERCURY-AR χ ES**.

2.1.1. Header, threading and scheduling

All subroutines that take advantage of OpenMP parallelization start with the following header:

```
!$ use OMP_LIB
!$ include 'openmp.inc'
```

Both statements are inserted as optional programming commands, meaning that they are treated as comments when the source code is compiled serially. The explicit inclusion of the `USE OMP_LIB` statement ensures portability and consistent behavior across different compilers/OpenMP implementations.

The inclusion of the file `OPENMP.INC` imports into the subroutines the declarations of three variables controlling the parallel execution of the code at runtime:

- `N_TH`, an integer constant setting the number of threads to be used when running in parallel;
- `OMP_DYNFLAG`, a boolean constant that allows for switching between static scheduling and dynamic scheduling in managing the parallel execution;
- `NPAR_TH`, an integer constant specifying the minimum number of body for parallel execution in case of conditional parallelization (see below).

At the beginning of each subroutine containing OpenMP parallel directives, the `N_TH` and `OMP_DYNFLAG` parameters are used to configure the runtime environment in terms of threading and

scheduling by calling the relevant subroutines provided by the OpenMP library as:

```
!$ call OMP_SET_NUM_THREADS(n_th)
!$ call OMP_SET_DYNAMIC(omp_dynflag)
```

With GNU compilers we experienced loss of performances when selecting the dynamic scheduler, while with Intel compilers the two choices did not show significant differences in terms of performances. Performance-wise, the safest choice for `OMP_DYNFLAG` is therefore the static scheduler. The parameter `NPAR_TH` is used instead whenever parallel instructions are used on a subset of bodies to prevent parallel functionalities from being used in situations where insufficient computational load may cause them to hinder performance, e.g. during the resolution of close encounters:

```
!$omp parallel do simd default(shared)
!$omp& private(tmp1,tmp2) if(nbod>npar_th)
  do k = 2,nbod
    tmp1 = x0(1,k)*x0(1,k)+x0(2,k)*x0(2,k)
    & +x0(3,k)*x0(3,k)
    tmp2 = v0(1,k)*v0(1,k)+v0(2,k)*v0(2,k)
    & +v0(3,k)*v0(3,k)
    xscal(k) = 1.d0/tmp1
    vscal(k) = 1.d0/tmp2
  end do
!$omp end parallel do simd
```

2.1.2. Parallel, Parallel SIMD and Critical regions

All loops and array operations that can benefit from parallelism have been enclosed in `PARALLEL DO` and `PARALLEL WORKSHARE` directives, as in the following code examples:

```
!$omp parallel do default(shared) private(temp)
  do j = 2, nbod
    xmin(j) = min (x0(1,j), x1(1,j))
    xmax(j) = max (x0(1,j), x1(1,j))
    ymin(j) = min (x0(2,j), x1(2,j))
    ymax(j) = max (x0(2,j), x1(2,j))
  c
  c If velocity changes sign, do an interpolation
    if ((v0(1,j).lt.0.and.v1(1,j).gt.0).or.
    & (v0(1,j).gt.0.and.v1(1,j).lt.0)) then
      temp=(v0(1,j)*x1(1,j)-v1(1,j)*x0(1,j)
    & -0.5d0*h*v0(1,j)*v1(1,j))/(v0(1,j)
    & -v1(1,j))
      xmin(j) = min (xmin(j),temp)
      xmax(j) = max (xmax(j),temp)
    end if
  c
    if ((v0(2,j).lt.0.and.v1(2,j).gt.0).or.
    & (v0(2,j).gt.0.and.v1(2,j).lt.0)) then
      temp=(v0(2,j)*x1(2,j)-v1(2,j)*x0(2,j)
    & -0.5d0*h*v0(2,j)*v1(2,j))/(v0(2,j)
    & -v1(2,j))
      ymin(j) = min (ymin(j),temp)
      ymax(j) = max (ymax(j),temp)
```

```

    end if
  end do
!$omp end parallel do

```

and

```

!$omp parallel workshare
  ejcount=count(stat(:).lt.0)
!$omp end parallel workshare
  if (ejcount.gt.0) ejflag = 1

```

To maximize the performance consistency across different platforms and compilers, all parallel loops that can benefit from both parallelization and vectorization have been enclosed within PARALLEL DO SIMD directives:

```

!$omp parallel do simd default(shared)
  do j = 2, nbod
    v(1,j)=v(1,j)+hby2*(angf(1,j)
  & +ausr(1,j)+a(1,j))
    v(2,j)=v(2,j)+hby2*(angf(2,j)
  & +ausr(2,j)+a(2,j))
    v(3,j)=v(3,j)+hby2*(angf(3,j)
  & +ausr(3,j)+a(3,j))
  end do
!$omp end parallel do simd

```

The rationale of this choice is illustrated by the different philosophies of the two mainstream Intel and GNU suite of compilers. While Intel compilers implicitly analyze and vectorize parallel loops to maximize performance, GNU compilers disable implicit vectorization within parallel loops unless explicitly instructed to do so to minimize race conditions and the risk of producing incorrect results. The inclusion of the PARALLEL DO SIMD directives instructs the compiler that it is safe to combine parallelization and SIMD instructions.

During the profiling and assessment of the parallelization potential of the MERCURY n-body library, we identified two code regions that can prove computationally intensive in planet formation simulations but where the structure of the algorithms implemented in MERCURY prevents their straightforward parallelization. The first code region is associated with the identification of pairs of bodies undergoing close encounters during the timestep and for which the use of the Bulirsh-Stoer integrator is required:

```

c If minimum separation is small enough,
c flag this as a possible encounter
  temp = min (d0,d1,d2min)
  if (temp.le.rc2) then
!$omp critical(ce_snif)
  ce(i) = 2
  ce(j) = 2
  nce = nce + 1
  ice(nce) = i
  jce(nce) = j
!$omp end critical(ce_snif)
  end if

```

The second code region is associated with the computation of the forces acting between such pairs of bodies during the close encounters with the Bulirsh-Stoer integrator, and could incur in race conditions in those cases when a single body has multiple close encounters during a timestep:

```

!$omp critical(fo_hkce)
  faci = tmp2 * m(i)
  facj = tmp2 * m(j)
  a(1,j) = a(1,j) - faci * dx
  a(2,j) = a(2,j) - faci * dy
  a(3,j) = a(3,j) - faci * dz
  a(1,i) = a(1,i) + facj * dx
  a(2,i) = a(2,i) + facj * dy
  a(3,i) = a(3,i) + facj * dz
!$omp end critical(fo_hkce)

```

In line with our philosophy of preserving the original structure of Mercury and the interoperability with legacy codes and libraries, we analyzed these code regions and verified that the issue could be efficiently addressed with the introduction of CRITICAL directives to take advantage of the sparse nature of close encounters and, consequently, access to the critical regions. While the two CRITICAL regions are located in different subroutines and there is currently no risk of race conditions, to prevent the chance of this occurrence in future updates we implemented them as named CRITICAL regions (see above).

2.1.3. Additional upgrades and features debugging

The source code of MERCURY+ also contains the following differences with respect to MERCURY (Chambers, 1999). First, we implemented the bug fix reported in de Souza Torres and Anderson (2008) by explicitly initializing the STAT variable in the subroutine MIO_IN. The STAT variable keeps track of the status of the bodies during the simulations and its explicit initialization prevents the compiler-dependent possibility of bodies being removed in a non-physical manner during or at the restart of simulations.

Second, we modified the loops computing the total momentum of the system in MCO_DH2H and MDT_HY and the loop computing the gravitational potential energy in MXX_EN to run only over the number of massive bodies rather than over the total number of bodies. This simple solution proved to be more effective than parallelizing the loops for the use cases investigated with the code (Turrini et al., 2019, 2021; Bernabò et al., 2022; Turrini et al., 2023; Polychroni et al., 2025; Sirono and Turrini, 2025). According to tests, parallelizing these loops is advised for simulations including more than 10^4 massive particles.

Third, we upgraded the MXX_SORT subroutine to support arrays up to $\approx 8 \times 10^5$ elements instead of the original $\approx 3 \times 10^4$ to prevent spurious behaviors in large simulations; the upgrade extends the gap sequence of Shellsort in the INCARR variable up to the 12th term following Knuth's method ($x = (3^n - 1)/2$, Knuth 1973):

```

data incarr/1,4,13,40,121,364,1093,3280,
& 9841,29524,88573,265720/

```

Finally, we modified the computation of Newtonian forces in the subroutine `MFO_DRCT` to branch automatically depending on whether the code is running in parallel or not, taking advantage of conditional directives. When the code is run serially, the variable `OPENMPFLAG` is set to `.FALSE.` and the original and more efficient triangular loop by `MERCURY` is used. When the code is run in parallel, the OpenMP directive setting `OPENMPFLAG` to `.TRUE.` is activated and a rectangular loop is used instead:

```

data openmpflag/ .false. /
!$ openmpflag=.true.
if (i0.le.0) i0 = 2
if (openmpflag.eqv..false.) then
  do i = i0, nbig
    do j = i + 1, nbod
      dx = x(1,j) - x(1,i)
      dy = x(2,j) - x(2,i)
      dz = x(3,j) - x(3,i)
      s2 = dx*dx + dy*dy + dz*dz
      rc = max(rcrit(i),rcrit(j))
      rc2 = rc * rc
      if (s2.ge.rc2) then
        s_1 = 1.d0 / sqrt(s2)
        tmp2 = s_1 * s_1 * s_1
      else if (s2.le.0.01*rc2) then
        tmp2 = 0.d0
      else
        s_1 = 1.d0 / sqrt(s2)
        s = 1.d0 / s_1
        s_3 = s_1 * s_1 * s_1
        q = (s - 0.1d0*rc) / (0.9d0 * rc)
        q2 = q * q
        q3 = q * q2
        q4 = q2 * q2
        q5 = q2 * q3
        tmp2=(10.d0*q3-15.d0*q4+6.d0*q5)
        *s_3
      end if
      faci = tmp2 * m(i)
      facj = tmp2 * m(j)
      a(1,j) = a(1,j) - faci * dx
      a(2,j) = a(2,j) - faci * dy
      a(3,j) = a(3,j) - faci * dz
      a(1,i) = a(1,i) + facj * dx
      a(2,i) = a(2,i) + facj * dy
      a(3,i) = a(3,i) + facj * dz
    end do
  end do
else
!$omp parallel do shared(x,rcrit,i0,nbig,nbod,m,a)
!$omp& private(i,j,dx,dy,dz,s2,rc,rc2,s_1,
!$omp& tmp2,s,s_3,q,q2,q3,q4,q5,faci,facj)
  do j = i0, nbod
    do i = i0, nbig
      if (i.ne.j) then
        dx = x(1,j) - x(1,i)
        dy = x(2,j) - x(2,i)

```

```

      dz = x(3,j) - x(3,i)
      s2 = dx*dx + dy*dy + dz*dz
      rc = max(rcrit(i), rcrit(j))
      rc2 = rc * rc
      c
      if (s2.ge.rc2) then
        s_1 = 1.d0 / sqrt(s2)
        tmp2 = s_1 * s_1 * s_1
      else if (s2.le.0.01*rc2) then
        tmp2 = 0.d0
      else
        s_1 = 1.d0 / sqrt(s2)
        s = 1.d0 / s_1
        s_3 = s_1 * s_1 * s_1
        q = (s - 0.1d0*rc) / (0.9d0 * rc)
        q2 = q * q
        q3 = q * q2
        q4 = q2 * q2
        q5 = q2 * q3
        tmp2=(10.d0*q3-15.d0*q4+6.d0*q5)
        *s_3
      end if
      faci = tmp2 * m(i)
      a(1,j) = a(1,j) - faci * dx
      a(2,j) = a(2,j) - faci * dy
      a(3,j) = a(3,j) - faci * dz
    end if
  end do
end do
!$omp end parallel do
end if

```

While theoretically less efficient than other solutions, e.g. collapsing the nested loops into a single one over pairs of bodies, this approach consistently provided the best performance.

3. Multi-physics engine of `MERCURY-ARXES`

The second component of `MERCURY-ARXES` is the `ARXES` library, which allows for modeling the physical processes involved in planet formation and the interactions of the planetary bodies with the surrounding protoplanetary disk. The library is composed of the following thematic Fortran95 modules and the main FORTRAN77 library:

- `ARXES_COMMON.F90`, a module library of astrophysical and conversion constants and mathematical functions used by the other modules;
- `ARXES_DISK.F90`, the module library containing the variables and initialization functions used for the computation of the interactions between the disk gas and the planetary bodies (Sect. 3.1);
- `ARXES_GROWTH.F90`, the module library containing the variables and subroutines implementing the mass growth and planetary radius evolution of forming planets (Sect. 3.2);

- ARXES_MIGRATION.F90, the module library containing the variables and subroutines implementing the orbital migration of forming planets (Sect. 3.3).
- ARXES.FOR, the main library, containing also modified versions of MERCURY subroutines in line with the preservation philosophy of MERCURY+ (Sects. 3.1,3.2,3.3).

In the following we detail the modeling algorithms and computational solutions adopted in the ARXES library.

3.1. Protoplanetary disks and dynamical effects of gas

The protoplanetary disk modeling assumes a viscous disk in steady state (Lynden-Bell and Pringle, 1974; Andrews et al., 2010) parametrized as

$$\Sigma_{\text{gas}}(r) = \Sigma_0 \left(\frac{r}{R_C} \right)^{-\gamma} \exp \left[- \left(\frac{r}{R_C} \right)^{2-\gamma} \right] \quad (1)$$

where R_C is the characteristic radius of the protoplanetary disk and the exponent γ sets the slope of the gas surface density distribution. The disk is truncated at the user-defined inner edge R_{in} and the gas density is set to zero inward of R_{in} .

The temperature profile in the disk midplane is characterized by the radial power law of irradiated disks (Hayashi, 1981; Isella et al., 2016):

$$T(r) = T_0 \left(\frac{R}{1 \text{ au}} \right)^{-\beta} K \quad (2)$$

where T_0 is the disk temperature at 1 AU and β is the slope of the temperature profile, both to be provided as input.

The density and temperature profiles of the disk from Eqs. 1 and 2 are used to compute the damping effects of the gas on the dynamical evolution of particles in the n-body simulations following Weidenschilling (1977). The drag acceleration F_D is:

$$F_D = \frac{3}{8} \frac{C_D \rho_g}{r_p \rho_p} \Delta v^2 \quad (3)$$

where C_D is the gas drag coefficient, ρ_g is the local volume density of the gas (Armitage, 2010), ρ_p and r_p are the average density and physical radius of the planetesimals, respectively, and Δv is the relative velocity between gas and planetesimals.

The volume density of the gas in the midplane is

$$\rho_g(r) = \frac{1}{\sqrt{2\pi}} \frac{\Sigma(r)}{h} \quad (4)$$

where $h = c_s/\Omega$ is the vertical disk scale-height, c_s and Ω are the isothermal sound speed and the orbital frequency at the orbital distance r (Armitage, 2010). The relative velocity Δv of the gas with respect to the local Keplerian velocity $v_k(r)$ is derived from the computation of the sub-Keplerian gas velocity following Brasser et al. (2007):

$$v_g(r) = v_k(r) \sqrt{1 - 2\eta(r)} \quad (5)$$

where $\eta(r)$ is

$$\eta(r) = \frac{1}{2\gamma_C} (\gamma + \beta/2 + 3/2) \left(\frac{c_s}{v_k} \right)^2 \quad (6)$$

where $\gamma_C = 7/5$ is the ratio of the specific heats of molecular hydrogen (Brasser et al., 2007).

The gas drag coefficient C_D of each planetesimal is computed following the treatment described by Tanigawa et al. (2014) as a function of the Reynolds (Re) and Mach (Ma) numbers (see Brasser et al., 2007, for the definitions adopted), coupling the individual drag coefficients to the specific orbit of the planetesimal and to the local disk environment:

$$C_D = \left[\left(\frac{24}{Re} + \frac{40}{10 + Re} \right)^{-1} + 0.23Ma \right]^{-2} + \frac{2 \cdot (0.8k + Ma)}{1.6 + Ma} \quad (7)$$

where k is a factor with value of 0.4 for $Re < 10^5$ and 0.2 for $Re > 10^5$ (Tanigawa et al., 2014; Nagasawa et al., 2019). This formulation of the drag coefficient C_D satisfies the condition of smooth transitions across different drag regimes as discussed by Stoyanovskaya et al. (2020).

After the onset of the runaway gas accretion phase (i.e. for $t > \tau_c$), giant planets are assumed to be surrounded by a gap with width Marzari (2018):

$$W_{\text{gap}} = C \cdot R_H \quad (8)$$

where the numerical proportionality factor $C = 4$ is from Marzari (2018). Following Turrini et al. (2021), the gas density in the gap $\Sigma_{\text{gap}}(r)$ evolves over time with respect to the local unperturbed gas density $\Sigma(r)$ as:

$$\Sigma_{\text{gap}}(r) = \Sigma(r) \cdot \exp \left[- (t - \tau_c) / \tau_g \right] \quad (9)$$

where τ_c and τ_g are the same as in Eqs. 13 and 15.

The effects of disk gravity on the orbital motion of planetesimals are computed through the analytical treatment for axisymmetric thin disks of Ward (1981), which Fontana and Marzari (2016) showed being in good agreement with the perturbations computed from hydrodynamic simulations. Following Nagasawa et al. (2019), the computation focuses on the leading term of the force due to disk gravity (F_{DG}) which, when $\gamma \neq 1$, is:

$$F_{DG} = 2\pi G \Sigma(r) \sum_{n=0}^{\infty} A_n \frac{(1-\gamma)(4n+1)}{(2n+2-\gamma)(2n-1+\gamma)} \quad (10)$$

where $A_n = [(2n)!/2^{2n}(n!)^2]^2$ (Ward, 1981; Marzari, 2018). When $\gamma = 1$, the numerator of the right-hand summation of Eq. 10 becomes zero, so the following leading term in the analytical formulation of Ward (1981) is computed instead:

$$F_{DG} = 2\pi G \Sigma(r) \sum_{n=0}^{\infty} A_n \frac{(2n+1)}{(2n+2-\gamma)} \left(\frac{R_{in}}{r} \right)^{2n+2-\gamma} \quad (11)$$

For all practical purposes $\frac{R_{in}}{r} < 1$ (see below) and the contribution of all terms for $n \geq 1$ rapidly goes to zero. Focusing on the leading term $n = 0$ the equation simplifies to

$$F_{DG} = 2\pi G \Sigma(r) \left(\frac{R_{in}}{r} \right) \quad (12)$$

Focusing on the leading terms that determine disk gravity is computationally efficient and has been shown to be accurate as long as the planetary bodies are distant from both the inner and outer edges of the disk (Fontana and Marzari, 2016). However, for all practical purposes this approach proves adequate also when this condition is not satisfied (Turrini et al., 2021).

In the inner disk regions, the dynamical evolution of planetesimals is dominated by the damping effects of gas drag that promptly cancel out any excitation due to the disk gravity. Numerical experiments including the additional terms required to account for the effects of the inner disk edge showed no appreciable difference in the dynamical evolution of the planetesimals (Turrini et al., 2021). Given the wider extension of the disk gas with respect to solids (Mordasini et al., 2016; Isella et al., 2016; Ansdell et al., 2018; Facchini et al., 2019), the only planetary bodies that approach the disk outer edge in typical planet formation simulations are those scattered into an extended disk or ejected from the planetary system by massive planets (Polychroni et al., 2025). For these bodies, the dominant contributions that shape their dynamical evolution are the close encounters with the massive planets, while the rapidly decreasing gas density limits the role of disk gravity.

3.1.1. HPC implementation of the interactions with the gas

Modeling the interactions between planetary bodies and disk gas is one of the most computationally demanding task in **MERCURY-AR χ ES** and, depending on the simulated planetary architecture, it can outweigh the computation of the Newtonian forces (see Sect. 4). The direct computation of Newtonian forces in **MERCURY** scales as $O(N_{big}N_{tot})$ where N_{big} is the number of massive bodies, $N_{tot} = (N_{small} + N_{big})$ and N_{small} is the number of massless particles. The interactions with the gas scale linearly on N_{tot} but are characterized by higher arithmetic intensity per body, β , globally scaling as $O(\beta N_{tot})$.

When the computational weight of β proves greater than that of N_{big} , e.g. when simulating few planetary bodies embedded into an extended planetesimal disk as in the use cases in Sect. 4, $O(\beta N_{tot})$ grows faster than $O(N_{big}N_{tot})$ and becomes the dominant contribution to the computational load of the simulation. It is therefore critical to ensure that the implementation of the gas-particle interactions benefits from both parallelization and vectorization. **MERCURY-AR χ ES** achieves this by pre-computing in separate loops all quantities associated to complex if-branches or non-contiguous stride in memory access that would prevent vectorization. The following code example showcases the identification of massless particles crossing the disk inner edge or the gaps surrounding forming planets, and the computation of multiplicative factors to correct the gas density they experience:

```
!$omp parallel do default(shared) private(i)
  do j = nbig+1,nbod
    if ((Rxyd(j).lt.inner_edge)) then
      dens_factor(j)=0.0d0
    else if (nbig.gt.1.and.growthflag
    & .eqv..true.) then
      do i = 2,nbig
        if ((growthflag2(i).eqv..true.).and.
```

```
& (time.gt.tstart2(i))) then
  if ((Rxyd(j).lt.(rpla(i)+gap_w(i)))
  .and.(Rxyd(j).gt.(rpla(i)-
  gap_w(i)))) then
    dens_factor(j)=exp(-(time-
    tstart2(i))/tfold2(i))
  end if
end if
end do
end if
end do
!$omp end parallel do
```

3.2. Growth of the forming planets

The growth of the planets is modeled using the two-phases parametric approach from Turrini et al. (2011, 2019), which allows fitting the growth tracks from physically realistic simulations based on planetesimal accretion (Lissauer et al., 2009; D’Angelo et al., 2021) and pebble accretion (Bitsch et al., 2015; Johansen et al., 2019).

The first phase reproduces the growth of the planet by accretion of solids and the subsequent capture of an extended primary atmosphere composed of disk gas. The duration of this phase is set by the timescale τ_c , during which the planetary mass M_p grows from the initial value M_0 to the final value M_c as

$$M_p = M_0 + \left(\frac{e}{e-1} \right) (M_c - M_0) (1 - e^{-t/\tau_c}) \quad (13)$$

The physical radius of the growing planet R_p evolves alongside the planetary mass following the approach described by Lissauer et al. (2009) and Fortier et al. (2013):

$$R_p = \frac{G M_p}{c_s^2/k_1 + (G M_p) / (k_2 R_H)} \quad (14)$$

where G is the gravitational constant, M_p and R_H are the instantaneous mass and Hill’s radius of the planet, respectively, c_s is the sound speed in the protoplanetary disk at the orbital distance of the planet, and $k_1 = 1$ and $k_2 = 1/4$ are constants (Lissauer et al., 2009). The parameters τ_c , M_0 and M_c are input values of the simulation.

The second phase reproduces the runaway gas accretion that allows the forming planet to become a gas giant. The mass growth during the runaway gas accretion is modeled as:

$$M_p = M_c + (M_f - M_c) (1 - e^{-(t-\tau_c)/\tau_g}) \quad (15)$$

where M_f is the final planetary mass while τ_g is the e-folding time of the runaway gas accretion. During the gravitational infall of the gas, the planetary radius shrink over time as:

$$R_p = R_c - \Delta R (1 - \exp^{-(t-\tau_c)/\tau_g}) \quad (16)$$

where R_c is the planetary radius at τ_c , i.e. the onset of the runaway accretion, and $\Delta R = R_c - R_I$ is the decrease of the planetary radius during the gravitational collapse of the gas. The parameters τ_g , M_f and ΔR are input values of the simulation.

3.3. Migration of the forming planets

The migration of the forming planets due to their interactions with the surrounding protoplanetary disk is modeled through the two-phases approach from Turrini et al. (2021), which in turn semi-analytically models the realistic non-isothermal migration tracks from the population synthesis models by Morrasini et al. (2015). The two migration phases are characterized by linear and power-law migration regimes, respectively, and are implemented based on the analytical treatment of Hahn and Malhotra (2005).

The first phase is described by a linear migration regime governed by the drift rate Δv_1 (Turrini et al., 2021):

$$\Delta v_1 = \frac{1}{2} \frac{\Delta a_1}{a_p} \frac{\Delta t}{\tau_1} v_k \quad (17)$$

where Δa_1 and τ_1 are the radial displacement and duration of this migration phase, v_k and a_p are the Keplerian velocity and semimajor axis of the planet, and Δt is the timestep used in the n-body simulations.

The second migration phase is described by a power law migration regime governed by the drift rate Δv_2 (Hahn and Malhotra, 2005):

$$\Delta v_2 = \frac{1}{2} \frac{\Delta a_2}{a_p} \frac{\Delta t}{\tau_2} \exp^{-(t-\tau_1)/\tau_2} v_k \quad (18)$$

where Δa_2 and τ_2 are the radial displacement and duration of this migration phase, while all other parameters are the same as those in Eq. 17.

From a physical point of view, the two migration regimes are coupled to the two growth phases discussed in Sect. 3.2 meaning that $\tau_1 = \tau_c$ and $\tau_2 = \tau_g$ (Turrini et al., 2021, 2023). The implementation of the two migration regimes, however, allows for decoupling orbital migration from planetary growth and introduce arbitrary user-defined migration histories, e.g. by delaying the onset of migration with respect to the onset of solid growth or extending the linear migration regime also during the gas accretion phase.

3.4. Planetesimal disk

MERCURY-ARXES models planetesimal disks as swarms of dynamical tracers possessing inertial mass but no gravitational mass. The lack of gravitational mass means that tracers do not affect each other nor the planets, behaving as massless particles at population level. The attribution of inertial mass allows for quantifying the way planetesimals are affected by the disk gas through the processes discussed in Sect. 3.1.

The inertial mass is quantified from the physical radius and the density of the planetesimals. The current implementation of MERCURY-ARXES allows for attributing in input the global characteristic radius of all planetesimals. The selection of the planetesimal density is currently hard-coded in MERCURY-ARXES: tracers whose initial semimajor axes position them inward of the water snowline are considered rocky and attributed an average density of $\rho_{rock}=2.4 \text{ g cm}^{-3}$ (Turrini et al. 2014 based on asteroid densities from Britt et al. 2002; Carry 2012). Tracers whose initial semimajor axes position them outward of the

water snowline are considered ice-rich and attributed an average density $\rho_{ice} = 1 \text{ g cm}^{-3}$ following Turrini et al. (2019). This value mediates between cometary densities (0.4-0.6 g cm⁻³, see Brasser et al. 2007 and references therein and Jorda et al. 2016) and the density of the 200 km-wide ice-rich Saturnian irregular satellite Phoebe (1.63 g cm⁻³, Porco et al. 2005).

3.5. Updated ejection criterion for planetary bodies

MERCURY-ARXES implements the physically-justified ejection criterion where planetary bodies are flagged for ejection when their orbits become physically unbound (i.e., the orbital eccentricity is greater or equal than unity; Polychroni et al. 2025), in place of the original criterion of MERCURY based on threshold orbital distances specified in input by the users. As the computation of the orbital elements is more expensive than that of the instantaneous radial distance, we parallelized the block of instructions as shown below:

```
!$omp parallel do simd default(shared)
|$omp& private(gm,q,ecc,inc,tmp1,tmp2,tmp3)
do j = i0, nbod
  if (j.le.nbig) then
    gm=m(1)+m(j)
  else
    gm=m(1)
  end if
  call mco_x2el (gm,x(1,j),x(2,j),x(3,j),
& v(1,j),v(2,j),v(3,j),q,ecc,inc,tmp1,
& tmp2,tmp3)
  if (ecc.ge.1.0d0) then
    stat(j) = -3
    m(j) = 0.d0
    s(1,j) = 0.d0
    s(2,j) = 0.d0
    s(3,j) = 0.d0
  end if
end do
!$omp end parallel do simd
```

3.6. Migration and time-step adapting

Depending on the adopted migration track, the forming planets in the simulations may reach the orbital regions close to the host star where correctly resolving the temporal evolution of the orbits requires extremely small timesteps. Adopting the necessary small timestep across the whole duration of the simulation would prove prohibitively expensive from a computational point of view. To effectively address this issue, MERCURY-ARXES allows the user to start the simulation with the optimal timestep for the input architecture and switch to the smaller timestep when required by automatizing the approach adopted by Jurić and Tremaine (2008).

When the planet approaches the orbital distance where the initial timestep proves too long to correctly sample the orbit, the n-body code decreases the timestep to 1/25 of the orbital period at the minimum semimajor axis specified in input. While the high numerical stability of the WHFAST Kepler solver (Rein and Tamayo, 2015) is expected to ensure the smooth transition

between the two timesteps, for increased accuracy MERCURY- $\text{\textit{ARXES}}$ applies the hybrid approach of MERCURY also during the timestep when the transition in dt occurs and computes the Keplerian orbital motion of the bodies requiring the updated timestep using the Bulirsh-Stoer integrator.

3.7. Temporal evolution of the planetary system

While the original output files of MERCURY are preserved for compatibility with existing legacy codes, MERCURY- $\text{\textit{ARXES}}$ introduces new output files in the form of sequential snapshots of the dynamical and physical state of the planetary system. During runtime, these files serve as quick-look windows on the real-time state of the simulated system. At the end of the simulations, they support the analysis of its global temporal evolution without the need of unpacking MERCURY’s output, which stores the evolution of each planetary body in individual files and requires processing an impractically large number of files in modern planet formation simulations.

The snapshots are timed by the same frequency of the data dumps for the creation of restart files, to guarantee the alignment of the outputs in the case of interruptions or when restarting the simulations. The snapshot files report the time of the snapshot in simulation time followed by the orbital information of all bodies, massive and massless. For all bodies the snapshots report the osculating main orbital elements - semimajor axis, eccentricity and inclination - followed by the initial semimajor axis a_0 , used to trace the formation region of the bodies, and the state vectors \vec{x} and \vec{v} . For the massive planets, the snapshots also report their radius and mass values.

4. Workload profile and code performance

MERCURY- $\text{\textit{ARXES}}$ is designed as a flexible investigation tool capable of adapting to the large diversity of observed architectures of planetary systems and of their stellar and disk formation environments (e.g. Zhu and Dong, 2021; Feinstein et al., 2025). This adaptability, on the other hand, means that workload profiles are system-dependent and there is no unique profile on which to tune MERCURY- $\text{\textit{ARXES}}$ ’s performance. When modeling planetary systems without migrating planets, in absence of large-scale dynamical instabilities close encounters will be comparatively sparse over the simulation duration and most of the workload will reside in the parallel regions. When modeling systems where planets undergo migration, close encounters will occur more frequently and will increase the relative computational load of the serial parts of the code, without necessarily activating their conditional parallelization. Moreover, as introduced in Sect. 3.1.1, depending on the relative numbers of massive and massless bodies in each simulation the workload profile can be dominated by the direct computation of the Newtonian forces or by the gas-bodies interactions.

In the following, we will focus on use cases from recent exoplanetary investigations performed with MERCURY- $\text{\textit{ARXES}}$ to illustrate and discuss the performance of the code. Specifically, we will adopt two use cases where giant planets form and migrate across extended planetesimal disks reaching compact final

Flat profile:						
Each sample counts as 0.01 seconds.						
% time	cumulative seconds	self seconds	calls	s/call	s/call	name
38.97	142.06	142.06	125151	0.00	0.00	arxes_gas
16.51	202.23	60.17	62099	0.00	0.01	arxes_gas
10.28	239.71	37.48	1070754069	0.00	0.00	reb_whfast_kepler_solver
7.58	267.33	27.62	1072702760	0.00	0.00	mco_x2el
4.40	283.38	16.05	436719	0.00	0.00	mco_dh2
3.96	297.80	14.42	125151	0.00	0.00	mfo_drct
3.10	309.11	11.31	2784721239	0.00	0.00	stiefel_gs3
2.72	319.04	9.93	252728	0.00	0.00	mce_box
2.34	327.57	8.53	62099	0.00	0.00	mce_snif
2.17	335.48	7.91	62099	0.00	0.00	mce_cent

Figure 1: Flat profile produced by GPROF for the serial run of MERCURY- $\text{\textit{ARXES}}$ described in Sect. 4.1. The simulated planetary system hosted two growing and migrating planets and about 18000 massless particle interacting with the disk gas. The flat profile shows the ten most computationally expensive subroutines.

orbits around their host stars. In both use cases, the giant planets start as lunar-mass planetary embryos ($0.01 M_{\oplus}$) to grow to Jupiter-like masses ($100-300 M_{\oplus}$), while the planetesimal disks are represented by swarms of massless particles embedded in protoplanetary disks with mass equal to 5% that of their central stars and interacting with the surrounding gas. The first use case will be used to analyze the performance of MERCURY- $\text{\textit{ARXES}}$ on consumer-grade infrastructures, while the second will be used to analyze its performance and scalability on high-end HPC nodes. Further details on the profiling of the code are provided in Simonetti et al., this issue, while information on the code runtime in the campaign of simulations of the OPAL project is provided in Polychroni et al., this issue.

4.1. Use case 1: Intel Performance Hybrid Architectures

The first analysis is performed on an HP Z2 G9 workstation running Linux Mint 21.3 and equipped with 12th Generation Intel Core i9-12900 and 64 GB of DDR5-4800 RAM. This processor is based on Intel Performance Hybrid Architecture and integrates two types of cores into a single die¹: Performance-cores (P-cores) and Efficient-cores (E-cores). P-cores are designed to maximize processing power, measured as instructions

¹<https://www.intel.com/content/www/us/en/products/sku/134597/intel-core-i912900-processor-30m-cache-up-to-5-10-ghz-specifications.html>

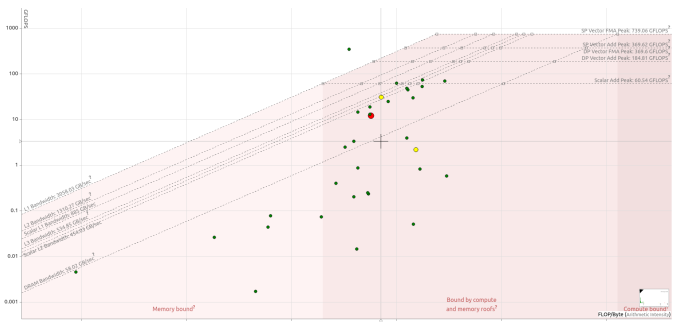


Figure 2: Roofline analysis produced by Intel Advisor for the parallel run of MERCURY- $\text{\textit{ARXES}}$ described in Sect. 4.1 using the same planetary system as Fig. 1. The red symbol is the most computationally intensive subroutine, ARXES_GAS, while the two yellow ones are MCO_X2EL and MCE_CENT (see discussion in Sect. 4.1 for details). The roofline plot highlights how most of the computational load of the simulation resides in the compute and memory bound region.

per cycle, and are capable of hyper-threading. E-cores are designed instead to maximize energy efficiency, measured as performance-per-watt, and are not capable of hyper-threading. The i9-12900 processor is equipped with 8 P-cores (physical cores: id. 0-7, hyper-threading virtual cores: id. 8-15) capable of turbo frequencies up to 5 GHz and 8 E-cores (physical cores: id. 16-23) capable of turbo frequencies up to 3.8 GHz. Performance hybrid architecture processors are equipped with two additional technologies that impact scalar and multi-thread performance: Intel Thread Director and Intel Turbo Boost Max 3.0. Intel Thread Director is capable of automatically routing the workload to the most efficient cores, hence dynamically optimizing the global workflow. Intel Turbo Boost Max 3.0, alongside boosting the clock frequencies of all cores, is capable of identifying up to two of the fastest cores on the processor and further boost their clock frequencies. The combination of these technologies with the Performance Hybrid Architecture of the processor may results in deviations between the performance of the code when run serially and with few threads with respect to when it is run with higher thread counts.

Based on the suggested flags of the PRACE Best Practice Guides² (Saastad et al., 2020), MERCURY- Δ XES is compiled with GFORTRAN 11 using the flags `-STD=LEGACY -OFAST -MARCH=CORE-AVX2 -MTUNE=CORE-AVX2 -MALIGN-DATA=CACHELINE -FLTO` (plus `-FOPENMP` when run in multithreaded mode), while WHFAST is compiled with GCC 11 using the flags `STD=c99 -O3 -MARCH=CORE-AVX2 -MTUNE=CORE-AVX2 -FLTO`. The use case adopted is based on one of the scenarios (id. 3) simulated by Turrini et al. (2023) and considers two forming giant planets starting respectively at 10 and 20 AU from the host star and a planetesimal disk extending from 1 to 25 AU composed of 1000 massless particles/au, for a total of about 18000 particles. We refer interested readers to Turrini et al. (2023) for additional details on the simulated planetary architecture and formation history. Since the use case focuses on the code performance rather than scientific accuracy, we considered simulation durations as well as formation and migration timescales 100-200 times shorter than in the original simulations from Turrini et al. (2023), meaning that each simulation spans 10^4 years, the planetary cores grow in 5×10^3 years and they undergo runaway gas accretion with a characteristic timescale of 10^3 years. This setup results in a serial runtime of 3703 seconds.

Before proceeding with the simulations, we performed two preliminary test runs, one serial and one running on eight threads on OpenMP, with timescales further reduced by a factor of 10, for a serial runtime of 364.54 seconds. The serial run was profiled with GPROF and produced the flat profile of Fig. 1, which shows the ten most computationally expensive subroutines. As discussed in Sect. 3.1.1, this use case is dominated by the computational cost of the interactions of the planetary bodies with the gas (Δ XES_GAS). The parallel run, where we let Intel Thread Director handle the distribution of the workload, was used to produce the roofline analysis of Fig. 2 using Intel Advisor. The resulting roofline plot reveals that the majority of the compu-

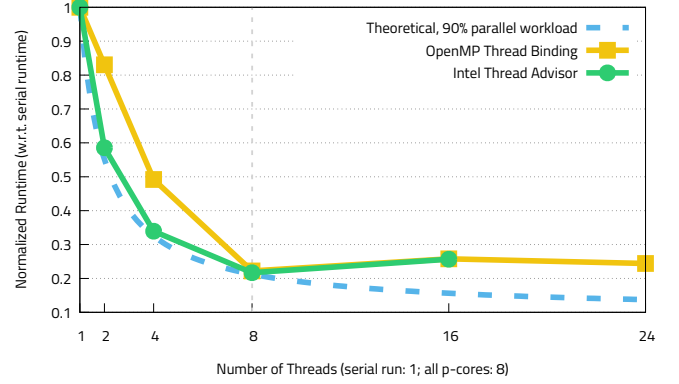


Figure 3: Comparison of the runtime values of MERCURY- Δ XES in the tests of Sect. 4.1 when running serially, in parallel with no thread binding (i.e. leaving the management of the workload schedule to the processor and the operating system) and in parallel with thread binding. All runtime values are normalized to the duration of the serial run. The theoretical dashed curve shows the expected runtime based on Amdahl’s law when 90% of the workload is parallelized. The vertical dashed line marks the number of P-cores available on the processor.

tational load of the simulation falls in the region characterized by both memory and compute bounds. The most computationally heavy subroutine remains Δ XES_GAS (red symbol in Fig. 2), followed by the conversion of state vectors into orbital elements (MCO_X2EL, top yellow symbol and the fourth entry in the flat profile of Fig. 1) and the computation of encounters with the central star (MCE_CENT, bottom yellow symbol and the tenth entry in the flat profile of Fig. 1). The latter two subroutines are implemented serially, but the calls to MCO_X2EL have been inserted wherever possible into parallel OpenMP DO loops, thus optimizing their use in the simulations.

We performed six simulations with the nominal setup adopted for this use case: a serial one and five parallel ones using 2, 4, 8, 16 and 24 cores. The first three parallel simulations run on P-cores, with Intel Thread Director deciding which cores to use between the physical and virtual ones. The simulation with 16 and 24 cores simultaneously make use of both P-cores and E-cores, with the case running on 24 cores also using hyper-threading. To test the computational implications of Performance Hybrid Architectures, we performed two sets of parallel simulations: the first set did not use any thread binding and relied on the operating system and Intel Thread Director to manage the workload distribution, while the second set implemented thread binding using the environmental variables `OMP_PROC_BIND="TRUE"` and `OMP_PLACES="THREADS"`. In the simulations with 2, 4 and 8 threads we forced the use of the P-cores setting `GOMP_CPU_AFFINITY=0-7`, while in the simulation with 16 threads we forced the use of P-cores and E-cores setting `GOMP_CPU_AFFINITY=0-7,16-23`. The results of the two sets of simulations are compared in Fig. 3 in terms of their normalized runtime with respect to the serial run. Fig. 3 also show the theoretical normalized runtime curve from Amdahl’s law when 90% of the total computational workload is parallelized.

The performance of the simulations running without thread

²<https://prace-ri.eu/resources/documentation/best-practice-guides/>

Particles	Execution	Runtime (hours)	Speedup
10000	Serial	86.07	4.76
	Parallel	18.07	
50000	Serial	290.6	5.94
	Parallel	48.86	

Table 1: Comparison of the serial and parallel runtime of MERCURY- $\text{\textit{ARX}}\text{\textit{ES}}$ on one node of Leonardo’s DCGP module for the test cases in Sect. 4.2 when simulating 1000 particles/au and 5000 particles/au. The parallel simulations are run with 14 threads using the version of MERCURY- $\text{\textit{ARX}}\text{\textit{ES}}$ containerized with Singularity adopted by the OPAL project (Polychroni et al., this issue). MERCURY- $\text{\textit{ARX}}\text{\textit{ES}}$ is compiled with Intel OneAPI using the compilation flags described in Sect. 4.2. The speedups of the parallel runs are consistent with 85-90% of the computational load being run in parallel. The average runtime/particle provides a measure of the computational efficiency of the code and shows that it improves moving from 1000 to 2000 particles/au and remains mostly constant for increasing numbers of particles.

binding follows exactly the theoretical curve with 90% parallel workload until all P-cores are used, while the simulations performed with thread binding using 2 and 4 cores visibly deviate from the theoretical expectations. Observing the core usage profile during runtime with and without thread binding hints to the explanation for these deviations. When the processor and the operating systems are allowed to decide which cores to use, the simulation with two threads run exclusively on two specific cores (virtual cores id. 8 and 13), likely those identified as top performing by Intel Turbo Boost Max 3.0. When thread binding is implemented, the specified pool of cores (physical cores id. 0-7) does not allow Intel Turbo Boost Max 3.0 to provide the additional frequency boost, resulting in lower performance with respect to the serial and unbounded parallel run. In the case of the simulation with 4 threads, the processor and operating system shift the workload between cores in a round-robin fashion but less frequently than observed in pre-Performance Hybrid Architecture processors. Furthermore, the top performing cores (id. 8 and 13) are used as often as possible but not in a continuous way. A plausible explanation is that the new technologies present on the processor successfully optimize the use of boosted frequencies and the thermal balance of the cores, while in the simulation run with thread-binding this is not feasible, resulting in degraded performance. The simulations running with 16 and 24 threads show lower performance than the case with 8 threads, with Intel Thread Director causing the simulation with 24 threads to stall without completing. This performance loss is likely caused by the compute and memory bound nature of the code, specifically the lower computational gain provided by the E-cores not compensating for the allocation of cache memory to the individual threads.

4.2. Use case 2: Leonardo Pre-Exascale Infrastructure

The second use case is run on the Leonardo Pre-Exascale Infrastructure³ using one node of its Data Centric General Purpose (DCGP) module. Each DCGP node is equipped with two 56-core Intel Xeon Platinum 8480+ CPUs and 512 GB of

DDR5-4800 RAM, with each core capable of turbo frequencies up to 3.8 GHz⁴. The use case follows the formation and migration of the giant planet WASP-69b around its host star and is derived from the *Origins of Planets for Ariel* (OPAL) project on Leonardo (Polychroni et al., this issue) in support of the ESA space mission Ariel (Tinetti et al., 2018). The giant planet starts the simulation as a lunar-mass planetary embryo ($0.01 M_{\oplus}$) located at 10 AU and ends its formation process at 0.4 AU with a mass of $81.05 M_{\oplus}$. During its growth and migration, the forming planet interacts with a planetesimal disk extending from 1 AU to 12.5 AU. While interacting with the forming planet, the planetesimal disk is affected by the protoplanetary disk within which it is embedded both in terms of aerodynamic drag and disk gravity. The host star has mass of $0.81 M_{\odot}$ while the mass of the protoplanetary disk is 5% of the stellar mass. The timestep of the simulations is 18 days and each simulation spanned a total duration of 1.5 Myr.

The setup of this use case implies that the forming planet interacts with a large number of planetesimals at each timestep, meaning that the CRITICAL code region responsible for the identification of the close encounters is called at most timesteps. Furthermore, at different timesteps the close encounters may be more effectively handled in serial than in parallel, meaning that the parallel fraction of the computational load fluctuates during runtime. Finally, the inclusion of only one forming planet reduces the computational weight of the Newtonian forces with respect to the first use case. To test how these characteristics of the use case affect performance and scalability, we run a set of parallel simulations with different number of particles and two serial ones. All simulations were run on a single node of the DCGP module of Leonardo, with MERCURY- $\text{\textit{ARX}}\text{\textit{ES}}$ being compiled with Intel OneAPI using the flags `-O3 -MARCH=CORE-AVX2 -ALIGN ARRAY64BYTE -FMA -IPO` (plus `-QOPENMP` when run in multi-threaded mode), while WHFAST is compiled using the flags `-STD=c99 -O3 -MARCH=CORE-AVX2 -FMA -IPO`. We considered four simulations using 1000, 2000, 5000 and 10000 particles/au to represent the planetesimal disks, resulting in total numbers of planetesimals of about 10000, 20000, 50000, 100000 massless particles. Each set of four simulations was run serially and in parallel with thread-binding using 14 threads per simulation. The parallel simulations were run with the same version of MERCURY- $\text{\textit{ARX}}\text{\textit{ES}}$ containerized with Singularity used in OPAL.

The wallclock runtime the serial and parallel simulations considering 10000 and 50000 particles are reported in Table 1. Their comparison reveals speedups of about a factor of 5 between serial and parallel simulations, with the run with 50000 particles proving overall more efficient. Using Amdahl’s law, the speedups reported in Table 1 are consistent with 85% of the workload being parallelized in the simulation with 10000 particles, while this percentage grows to about 90% in the simulation with 50000 particles. Fig. 4 shows the comparison of the total runtime (green curve with circles) and the average runtime per particle (golden curve with squares) of the four parallel simu-

³<https://leonardo-supercomputer.cineca.eu/hpc-system/>

⁴<https://www.intel.com/content/www/us/en/products/sku/231746/intel-xeon-platinum-8480-processor-105m-cache-2-00-ghz-specifications.html>

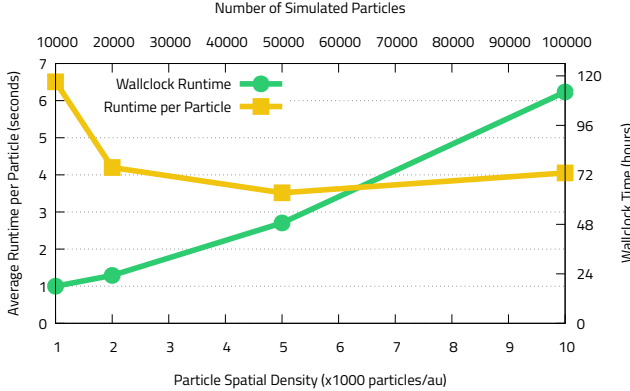


Figure 4: Comparison of the runtime of the parallel simulations of MERCURY-ARXES in Sect. 4.2. The simulations are run on one node of Leonardo’s DCGP module using 14 threads and considering planetesimal disks extending by about 10 AU and populated by 1000, 2000, 5000 and 10000 particles/au. The green curve with circle symbols shows the evolution of the wallclock runtime, the golden curve with square symbols shows the average runtime per particle. The parallel simulations are run with the version of MERCURY-ARXES containerized with Singularity adopted by the OPAL project (Polychroni et al., this issue). MERCURY-ARXES is compiled with Intel OneAPI using the compilation flags described in Sect. 4.2.

lations as a function of their increasing workload. The simulation with 10000 particles is the least efficient due to insufficient workload, in agreement with the information provided by Table 1. The average runtime per particle decreases when the computational workload increases: doubling the number of particles results in a limited runtime increase of about 30%, meaning that the overall computational efficiency grows. The normalized runtime/particles values in Fig. 4 confirm that the computational efficiency remains almost constant for larger workloads, the case with 50000 particles providing the best performance as discussed for Table 1.

5. Conclusions

In this work we described the high-performance implementation of the planet formation code MERCURY-ARXES and its underlying parallel n-body engine MERCURY+, which leverages on the OpenMP directive-based parallelism for shared memory environments to take advantage of the multi-thread and vectorization capabilities of modern processors. As we shown in summarizing its modeling capabilities and validating its performance in real use cases, MERCURY-ARXES provides a computationally efficient and physically realistic planet formation platform to simulate the multiple interactions between forming planets and their surrounding protoplanetary disk environments.

MERCURY-ARXES is available to the community through collaborations and is part of the Arxes suite of star and planet formation codes being used by the Key Science Project *Origins of Planets for ArieL* (OPAL) on the Leonardo Pre-Exascale Infrastructure (Polychroni et al., this issue) in support of ESA’s Ariel space mission (Tinetti et al., 2018). In the framework of the KSP OPAL, MERCURY-ARXES is also the foundation for MERCURY-OPAL, its porting to GPU computing based on the

OpenACC directive-based paradigm for heterogeneous computational infrastructures (Simonetti et al., this issue).

MERCURY+, the parallel n-body engine of MERCURY-ARXES, is available to the scientific community as stand-alone code upon request to the developing team, providing an enhanced, high-performance version of the widely used MERCURY code (Chambers, 1999). The design of both codes ensures seamless compatibility with existing additional n-body libraries, e.g. the DPI library to model planetary systems in binary star systems (Turriini, 2015; Nigoni et al., 2025), and with any legacy code developed by the community to interact with MERCURY.

Acknowledgments

The authors thank the original author of MERCURY John E. Chambers for providing the foundation for MERCURY+, and Francesco Marzari, Patricia Verrier, Nader Haghhighipour, Sinti Sironi, Martina Vicinanza and Eduard Vorobyov, as well as many participants to the MIAPbP workshop “Planet Formation: From Dust Coagulation to Final Orbit Assembly” held in 2022 in Garching, for the feedback and interactions that allowed the enhancement and validation of MERCURY-ARXES over the years. This work is supported by the Fondazione ICSC, Spoke 3 “Astrophysics and Cosmos Observations”, National Recovery and Resilience Plan (Piano Nazionale di Ripresa e Resilienza, PNRR) Project ID CN_00000013 “Italian Research Center on High-Performance Computing, Big Data and Quantum Computing” funded by MUR Missione 4 Componente 2 Investimento 1.4: Potenziamento strutture di ricerca e creazione di “campioni nazionali di R&S (M4C2-19)” - Next Generation EU (NGEU). The authors acknowledge support from ASI-INAF grant no. 2021-5-HH.0 plus addenda no. 2021-5-HH.1-2022 and 2021-5-HH.2-2024 and grant no. 2016-23-H.0 plus addendum no. 2016-23-H.2-2021, from the INAF-IFSI Basic Research projects *High Performance Planetology* (HPP), *High Performance Planetology - Second Edition* (HPP-2E), the INAF PRIN GENESIS-SKA and PLATEA, the INAF Main Stream project “Ariel and the astrochemical link between circumstellar discs and planets” (CUP: C54I19000700005), and the European Research Council via the Horizon 2020 Framework Programme ERC Synergy “ECOGAL” Project GA-855130. The authors also acknowledge the support of Amazon Web Services in the form of time allocation on their AWS EC2 infrastructure in the framework of the INAF-ICT2018 project. The authors wish to thank Vega Forneris, Francesco Reale and Mirko Riazoli for their support in managing the HPP and Genesis computational clusters at INAF, the development and validation platforms of MERCURY-ARXES. This research has made use of the Astrophysics Data System, funded by NASA under Cooperative Agreement 80NSSC21M00561

References

Andrews, S.M., Wilner, D.J., Hughes, A.M., Qi, C., Dullemond, C.P., 2010. Protoplanetary Disk Structures in Ophiuchus. II. Extension to Fainter Sources. *ApJ*

723, 1241–1254. doi:10.1088/0004-637X/723/2/1241, arXiv:1007.5070.

Ansdell, M., Williams, J.P., Trapman, L., van Terwisga, S.E., Facchini, S., Manara, C.F., van der Marel, N., Miotello, A., Tazzari, M., Hogerheijde, M., Guidi, G., Testi, L., van Dishoeck, E.F., 2018. ALMA Survey of Lupus Protoplanetary Disks. II. Gas Disk Radii. *ApJ* 859, 21. doi:10.3847/1538-4357/aab890, arXiv:1803.05923.

Armitage, P.J., 2010. *Astrophysics of Planet Formation*.

Bernabò, L.M., Turrini, D., Testi, L., Marzari, F., Polychroni, D., 2022. Dust Resurgence in Protoplanetary Disks Due to Planetesimal-Planet Interactions. *ApJ* 927, L22. doi:10.3847/2041-8213/ac574e.

Bitsch, B., Lambrechts, M., Johansen, A., 2015. The growth of planets by pebble accretion in evolving protoplanetary discs. *A&A* 582, A112. doi:10.1051/0004-6361/201526463, arXiv:1507.05209.

Bolmont, E., Raymond, S.N., Leconte, J., Hersant, F., Correia, A.C.M., 2015. Mercury-T: A new code to study tidally evolving multi-planet systems. Applications to Kepler-62. *A&A* 583, A116. doi:10.1051/0004-6361/201525909, arXiv:1507.04751.

Brasser, R., Duncan, M.J., Levison, H.F., 2007. Embedded star clusters and the formation of the Oort cloud. II. The effect of the primordial solar nebula. *Icarus* 191, 413–433. doi:10.1016/j.icarus.2007.05.003.

Britt, D.T., Yeomans, D., Housen, K., Consolmagno, G., 2002. Asteroid Density, Porosity, and Structure, in: W. F. Bottke Jr., A. Cellino, P. Paolicchi, and R. P. Binzel (Ed.), *Asteroids III*. University of Arizona Press, Tucson, AZ, pp. 485–500.

Carry, B., 2012. Density of asteroids. *Planet. Space Sci.* 73, 98–118. doi:10.1016/j.pss.2012.03.009, arXiv:1203.4336.

Chambers, J.E., 1999. A hybrid symplectic integrator that permits close encounters between massive bodies. *MNRAS* 304, 793–799. doi:10.1046/j.1365-8711.1999.02379.x.

Chambers, J.E., Quintana, E.V., Duncan, M.J., Lissauer, J.J., 2002. Symplectic Integrator Algorithms for Modeling Planetary Accretion in Binary Star Systems. *AJ* 123, 2884–2894. doi:10.1086/340074.

D’Angelo, G., Weidenschilling, S.J., Lissauer, J.J., Bodenheimer, P., 2021. Growth of Jupiter: Formation in disks of gas and solids and evolution to the present epoch. *Icarus* 355, 114087. doi:10.1016/j.icarus.2020.114087, arXiv:2009.05575.

de Souza Torres, K., Anderson, D.R., 2008. Symplectic Integrator Mercury: Bug Report. arXiv e-prints, arXiv:0808.0483doi:10.48550/arXiv.0808.0483, arXiv:0808.0483.

Emsenhuber, A., Mordasini, C., Burn, R., Alibert, Y., Benz, W., Asphaug, E., 2021. The New Generation Planetary Population Synthesis (NGPPS). I. Bern global model of planet formation and evolution, model tests, and emerging planetary systems. *A&A* 656, A69. doi:10.1051/0004-6361/202038553, arXiv:2007.05561.

Facchini, S., van Dishoeck, E.F., Manara, C.F., Tazzari, M., Maud, L., Cazzoletti, P., Rosotti, G., van der Marel, N., Pinilla, P., Clarke, C.J., 2019. High gas-to-dust size ratio indicating efficient radial drift in the mm-faint CX Tauri disk. *A&A* 626, L2. doi:10.1051/0004-6361/201935496, arXiv:1905.09204.

Feinstein, A.D., Booth, R.A., Bergner, J.B., Lothringer, J.D., Matthews, E.C., Welbanks, L., Miguel, Y., Bitsch, B., Eriksen, L.E.J., Kirk, J., Pelletier, S., Penzlin, A.B.T., Piette, A.A.A., Piaulet-Ghorayeb, C., Schwarz, K., Turrini, D., Acuña-Aguirre, L., Ahrer, E.M., Barber, M.G., Brande, J., Chakrabarty, A., Crossfield, I.J.M., Marleau, G.D., Huang, H., Johansen, A., Kreidberg, L., Livingston, J.H., Luque, R., Oreshenko, M., Pacetti, E., Perotti, G., Polman, J., Prinot, B., Semenov, D.A., Simon, J.B., Teske, J., Whiteford, N., 2025. On Linking Planet Formation Models, Protoplanetary Disk Properties, and Mature Gas Giant Exoplanet Atmospheres. arXiv e-prints, arXiv:2506.00669doi:10.48550/arXiv.2506.00669, arXiv:2506.00669.

Fenucci, M., Novaković, B., 2022. MERCURY and ORBIT Packages for Numerical Integration of Planetary Systems: Implementation of the Yarkovsky and YORP Effects. *Serbian Astronomical Journal* 204, 51–63. doi:10.2298/SAJ2204051F, arXiv:2202.13656.

Fontana, A., Marzari, F., 2016. Pericenter precession induced by a circumstellar disk on the orbit of massive bodies: comparison between analytical predictions and numerical results. *A&A* 589, A133. doi:10.1051/0004-6361/201527610.

Fonte, S., Turrini, D., Pacetti, E., Schisano, E., Molinari, S., Polychroni, D., Politi, R., Changeat, Q., 2023. Oxygen depletion in giant planets with different formation histories. *MNRAS* 520, 4683–4695. doi:10.1093/mnras/stad245, arXiv:2301.08616.

Fortier, A., Alibert, Y., Carron, F., Benz, W., Dittkrist, K.M., 2013. Planet formation models: the interplay with the planetesimal disc. *A&A* 549, A44. doi:10.1051/0004-6361/201220241, arXiv:1210.4009.

Grimm, S.L., Stadel, J.G., 2014. The GENGA Code: Gravitational Encounters in N-body Simulations with GPU Acceleration. *ApJ* 796, 23. doi:10.1088/0004-637X/796/1/23, arXiv:1404.2324.

Grimm, S.L., Stadel, J.G., Brasser, R., Meier, M.M.M., Mordasini, C., 2022. GENGA. II. GPU Planetary N-body Simulations with Non-Newtonian Forces and High Number of Particles. *ApJ* 932, 124. doi:10.3847/1538-4357/ac6dd2, arXiv:2201.10058.

Hahn, J.M., Malhotra, R., 2005. Neptune's Migration into a Stirred-Up Kuiper Belt: A Detailed Comparison of Simulations to Observations. *AJ* 130, 2392–2414. doi:10.1086/452638, arXiv:astro-ph/0507319.

Hayashi, C., 1981. Structure of the Solar Nebula, Growth and Decay of Magnetic Fields and Effects of Magnetic and Turbulent Viscosities on the Nebula. *Progress of Theoretical Physics Supplement* 70, 35–53. URL: <https://doi.org/10.1143/PTPS.70.35>, doi:10.1143/PTPS.70.35.

Isella, A., Guidi, G., Testi, L., Liu, S., Li, H., Li, S., Weaver, E., Boehler, Y., Carpenter, J.M., De Gregorio-Monsalvo, I., Manara, C.F., Natta, A., Pérez, L.M., Ricci, L., Sargent, A., Tazzari, M., Turner, N., 2016. Ringed Structures of the HD 163296 Protoplanetary Disk Revealed by ALMA. *Phys. Rev. Lett.* 117, 251101. doi:10.1103/PhysRevLett.117.251101.

Johansen, A., Ida, S., Brasser, R., 2019. How planetary growth outperforms migration. *A&A* 622, A202. doi:10.1051/0004-6361/201834071, arXiv:1811.00523.

Jorda, L., Gaskell, R., Capanna, C., Hviid, S., Lamy, P., Durech, J., Faury, G., Groussin, O., Gutiérrez, P., Jackman, C., Keihm, S.J., Keller, H.U., Knollenberg, J., Kührt, E., Marchi, S., Mottola, S., Palmer, E., Schloerb, F.P., Sierks, H., Vincent, J.B., A'Hearn, M.F., Barbieri, C., Rodrigo, R., Koschny, D., Rickman, H., Barucci, M.A., Bertaux, J.L., Bertini, I., Cremonese, G., Da Deppo, V., Davidsen, B., Debei, S., De Cecco, M., Fornasier, S., Fulle, M., Güttler, C., Ip, W.H., Kramm, J.R., Küppers, M., Lara, L.M., Lazzarin, M., Lopez Moreno, J.J., Marzari, F., Naletto, G., Oklay, N., Thomas, N., Tubiana, C., Wenzel, K.P., 2016. The global shape, density and rotation of Comet 67P/Churyumov-Gerasimenko from preperihelion Rosetta/OSIRIS observations. *Icarus* 277, 257–278. doi:10.1016/j.icarus.2016.05.002.

Jurić, M., Tremaine, S., 2008. Dynamical Origin of Extrasolar Planet Eccentricity Distribution. *ApJ* 686, 603–620. doi:10.1086/590047, arXiv:astro-ph/0703160.

Kinoshita, H., Yoshida, H., Nakai, H., 1991. Symplectic integrators and their application to dynamical astronomy. *Celestial Mechanics and Dynamical Astronomy* 50, 59–71.

Knuth, D.E., 1973. The art of computer programming. Vol.3: Sorting and searching.

Lissauer, J.J., Barnes, J.W., Chambers, J.E., 2012. Obliquity variations of a moonless Earth. *Icarus* 217, 77–87. doi:10.1016/j.icarus.2011.10.013.

Lissauer, J.J., Hubickyj, O., D'Angelo, G., Bodenheimer, P., 2009. Models of Jupiter's growth incorporating thermal and hydrodynamic constraints. *Icarus* 199, 338–350. doi:10.1016/j.icarus.2008.10.004, arXiv:0810.5186.

Lynden-Bell, D., Pringle, J.E., 1974. The evolution of viscous discs and the origin of the nebular variables. *MNRAS* 168, 603–637. doi:10.1093/mnras/168.3.603.

Marzari, F., 2018. Shifting of the resonance location for planets embedded in circumstellar disks. *A&A* 611, A37. doi:10.1051/0004-6361/201732070, arXiv:1712.04178.

Mordasini, C., Mollière, P., Dittkrist, K.M., Jin, S., Alibert, Y., 2015. Global models of planet formation and evolution. *International Journal of Astrobiology* 14, 201–232. doi:10.1017/S1473550414000263, arXiv:1406.5604.

Mordasini, C., van Boekel, R., Mollière, P., Henning, T., Benneke, B., 2016. The Imprint of Exoplanet Formation History on Observable Present-day Spectra of Hot Jupiters. *ApJ* 832, 41. doi:10.3847/0004-637X/832/1/41, arXiv:1609.03019.

Nagasawa, M., Tanaka, H., Ida, S., 2000. Orbital Evolution of Asteroids during Depletion of the Solar Nebula. *AJ* 119, 1480–1497. doi:10.1086/301246.

Nagasawa, M., Tanaka, K.K., Tanaka, H., Nomura, H., Nakamoto, T., Miura, H., 2019. Shock-generating Planetesimals Perturbed by a Giant Planet in a Gas Disk. *ApJ* 871, 110. doi:10.3847/1538-4357/aaf795.

Nigioni, A., Turrini, D., Danielski, C., Polychroni, D., Chambers, J.E., 2025. The quest for Magrathea planets. II. Orbital stability of exoplanets formed around double white dwarfs. arXiv e-prints , arXiv:2512.14460doi:10.48550/arXiv.2512.14460, arXiv:2512.14460.

Pacetti, E., Turrini, D., Schisano, E., Molinari, S., Fonte, S., Politi, R., Hennebelle, P., Klessen, R., Testi, L., Lebreuilly, U., 2022. Chemical Diversity in Protoplanetary Disks and Its Impact on the Formation History of Giant Planets. *ApJ* 937, 36. doi:10.3847/1538-4357/ac8b11, arXiv:2206.14685.

Polychroni, D., Turrini, D., Ivanovski, S., Marzari, F., Testi, L., Politi, R., Sozzetti, A., Trigo-Rodriguez, J.M., Desidera, S., Drozdovskaya, M.N., Fonte, S., Molinari, S., Naponiello, L., Pacetti, E., Schisano, E., Simonetti, P., Zusi, M., 2025. HD 163296 and its giant planets: Creation of exocomets, interstellar objects and transport of volatile material. *A&A* 697, A158. doi:10.1051/0004-6361/202453097, arXiv:2503.04669.

Porco, C.C., Baker, E., Barbara, J., Beurle, K., Brahic, A., Burns, J.A., Charnoz, S., Cooper, N., Dawson, D.D., Del Genio, A.D., Denk, T., Dones, L., Dyudina, U., Evans, M.W., Giese, B., Grazier, K., Helfenstein, P., Ingersoll, A.P., Jacobson, R.A., Johnson, T.V., McEwen, A., Murray, C.D., Neukum, G., Owen, W.M., Perry, J., Roatsch, T., Spitale, J., Squyres, S., Thomas, P.C., Tiscareno, M., Turtle, E., Vasavada, A.R., Veverka, J., Wagner, R., West, R., 2005. Cassini Imaging Science: Initial Results on Phoebe and Iapetus. *Science* 307, 1237–1242. doi:10.1126/science.1107981.

Rein, H., Liu, S.F., 2012. REBOUND: an open-source multi-purpose N-body code for collisional dynamics. *A&A* 537, A128. doi:10.1051/0004-6361/201118085, arXiv:1110.4876.

Rein, H., Tamayo, D., 2015. WHFAST: a fast and unbiased implementation of a symplectic Wisdom-Holman integrator for long-term gravitational simulations. *MNRAS* 452, 376–388. doi:10.1093/mnras/stv1257, arXiv:1506.01084.

Saastad, O.W., Kapanova, K., Markov, S., Morales, C., Shamakina, A., Johnson, N., Krishnasamy, E., Varrette, S., Shoukourian, H., 2020. PRACE Best Practice Guide 2020: Modern Processors. Technical Report. PRACE aisbl. URL: <https://prace-ri.eu/training-support/best-practice-guides/modern-processors/>. pdf.

Safronov, V.S., 1972. Evolution of the protoplanetary cloud and formation of the earth and planets.

Shibata, S., Helled, R., Ikoma, M., 2020. The origin of the high metallicity of close-in giant exoplanets. Combined effects of resonant and aerodynamic shepherding. *A&A* 633, A33. doi:10.1051/0004-6361/201936700, arXiv:1911.02292.

Shibata, S., Ikoma, M., 2019. Capture of solids by growing proto-gas giants: effects of gap formation and supply limited growth. *MNRAS* 487, 4510–4524. doi:10.1093/mnras/stz1629, arXiv:1906.05530.

Sirono, S.i., Turrini, D., 2025. Chondrule formation by collisions of planetesimals containing volatiles triggered by Jupiter's formation. *Scientific Reports* 15, 30919. doi:10.1038/s41598-025-12643-x.

Stoyanovskaya, O.P., Okladnikov, F.A., Vorobyov, E.I., Pavlyuchenkov, Y.N., Akimkin, V.V., 2020. Simulations of Dynamical Gas-Dust Circumstellar Disks: Going Beyond the Epstein Regime. *Astronomy Reports* 64, 107–125. doi:10.1134/S1063772920010072, arXiv:2102.09155.

Tanigawa, T., Maruta, A., Machida, M.N., 2014. Accretion of Solid Materials onto Circumplanetary Disks from Protoplanetary Disks. *ApJ* 784, 109. doi:10.1088/0004-637X/784/2/109, arXiv:1401.4218.

Tinetti, G., Drossart, P., Eccleston, P., Hartogh, P., Heske, A., Leconte, J., Micela, G., Ollivier, M., Pilbratt, G., Puig, L., Turrini, D., Vandenbussche, B., Wolkenberg, P., Beaulieu, J.P., Buchave, L.A., Ferus, M., Griffin, M., Guedel, M., Justtanont, K., Lagage, P.O., Machado, P., Malaguti, G., Min, M., Nørgaard-Nielsen, H.U., Rataj, M., Ray, T., Ribas, I., Swain, M., Szabo, R., Werner, S., Barstow, J., Burleigh, M., Cho, J., du Foresto, V.C., Coustenis, A., Decin, L., Encrenaz, T., Galand, M., Gillon, M., Helled, R., Morales, J.C., Muñoz, A.G., Moneti, A., Pagano, I., Pascale, E., Piccioni, G., Pinfield, D., Sarkar, S., Selsis, F., Tennyson, J., Triaud, A., Venot, O., Waldmann, I., Waltham, D., Wright, G., Amiaux, J., Auguères, J.L., Berthé, M., Bezwada, N., Bishop, G., Bowles, N., Coffey, D., Colomé, J., Crook, M., Crouzet, P.E., Da Peppo, V., Sanz, I.E., Focardi, M., Frericks, M., Hunt, T., Kohley, R., Middleton, K., Morgante, G., Ottenamer, R., Pace, E., Pearson, C., Stamper, R., Symonds, K., Rengel, M., Renotte, E., Ade, P., Affer, L., Alard, C., Alard, N., Altieri, F., André, Y., Arena, C., Argyriou, I., Aylward, A., Baccani, C., Bakos, G., Banaszkiewicz, M., Barlow, M., Batista, V., Bellucci, G., Benatti, S., Bernardi, P., Bézard, B., Blecka, M., Bolmont, E., Bonfond, B., Bonito, R., Bonomo, A.S., Brucato, J.R., Brun, A.S., Bryson, I., Bujwan, W., Casewell, S., Charnay, B., Pestellini, C.C., Chen, G., Ciaravella, A., Claudi, R., Clédassou, R., Damasso, M., Damiano, M., Danielski, C., Deroo, P., Di Giorgio, A.M., Dominik, C., Doublier, V., Doyle, S., Doyon, R., Drummond, B., Duong, B., Eales, S., Edwards, B., Farina, M., Flaccomio, E., Fletcher, L., Forget, F., Fossey, S., Fränz, M., Fujii, Y., García-Piquer, Á., Gear, W., Geoffray, H., Gérard, J.C., Gesa, L., Gomez, H., Graczyk, R., Griffith, C., Grodent, D., Guarcello, M.G., Gustin, J., Hamano, K., Hargrave, P., Hello, Y., Heng, K., Herrero, E., Hornstrup, A., Hubert, B., Ida, S., Ikoma, M., Iro, N., Irwin, P., Jarchow, C., Jaubert, J., Jones, H., Julien, Q., Kameda, S., Kerschbaum, F., Kervella, P., Koskinen, T., Krijger, M., Krupp, N., Lafarga, M., Landini, F., Lellouch, E., Leto, G., Luntzer, A., Rank-Lüftinger, T., Maggio, A., Maldonado, J., Maillard, J.P., Mall, U., Marquette, J.B., Mathis, S., Maxted, P., Matsuo, T., Medvedev, A., Miguel, Y., Minier, V., Morello, G., Mura, A., Narita, N., Nascimbeni, V., Nguyen Tong, N., Noce, V., Oliva, F., Palle, E., Palmer, P., Pancrazzi, M., Papageorgiou, A., Parmentier, V., Perger, M., Petralia, A., Pezzuto, S., Pierrehumbert, R., Pillitteri, I., Piotto, G., Pisano, G., Prisinzano, L., Radioti, A., Réess, J.M., Rezac, L., Rocchetto, M., Rosich, A., Sanna, N., Santerne, A., Savini, G., Scandariato, G., Sicardy, B., Sierra, C., Sindoni, G., Skup, K., Snellen, I., Sobiecki, M., Soret, L., Sozzetti, A., Stiepen, A., Strugarek, A., Taylor, J., Taylor, W., Terenzi, L., Tessenyi, M., Tsiaras, A., Tucker, C., Valencia, D., Vasish, G., Vazan, A., Vilardell, F., Vinatier, S., Viti, S., Waters, R., Wawer, P., Wawrzaszek, A., Whitworth, A., Yung, Y.L., Yurchenko, S.N., Osorio, M.R.Z., Zellem, R., Zingales, T., Zwart, F., 2018. A chemical survey of exoplanets with ARIEL. *Experimental Astronomy* 46, 135–209. doi:10.1007/s10686-018-9598-x.

Turrini, D., 2015. DPI: Symplectic mapping for binary star systems for the Mercury software package. *Astrophysics Source Code Library*, record ascl:1504.012. arXiv:1504.012.

Turrini, D., Codella, C., Danielski, C., Fedele, D., Fonte, S., Garufi, A., Guarcello, M.G., Helled, R., Ikoma, M., Kama, M., Kimura, T., Kruijssen, J.M.D., Maldonado, J., Miguel, Y., Molinari, S., Nikolaou, A., Oliva, F., Panić, O., Pignatari, M., Podio, L., Rickman, H., Schisano, E., Shibata, S., Vazan, A., Wolkenberg, P., 2022. Exploring the link between star and planet formation with Ariel. *Experimental Astronomy* 53, 225–278. doi:10.1007/s10686-021-09754-4, arXiv:2108.11869.

Turrini, D., Combe, J.P., McCord, T.B., Oklay, N., Vincent,

J.B., Prettyman, T.H., McSween, H.Y., Consolmagno, G.J., De Sanctis, M.C., Le Corre, L., Longobardo, A., Palomba, E., Russell, C.T., 2014. The contamination of the surface of Vesta by impacts and the delivery of the dark material. *Icarus* 240, 86–102. doi:10.1016/j.icarus.2014.02.021, arXiv:1401.6152.

Turri, D., Coradini, A., Magni, G., 2012. Jovian Early Bombardment: Planetesimal Erosion in the Inner Asteroid Belt. *ApJ* 750, 8. doi:10.1088/0004-637X/750/1/8, arXiv:1202.4887.

Turri, D., Magni, G., Coradini, A., 2011. Probing the history of Solar system through the cratering records on Vesta and Ceres. *MNRAS* 413, 2439–2466. doi:10.1111/j.1365-2966.2011.18316.x, arXiv:0902.3579.

Turri, D., Marzari, F., Polychroni, D., Claudi, R., Desidera, S., Mesa, D., Pinamonti, M., Sozzetti, A., Suárez Mascareño, A., Damasso, M., Benatti, S., Malavolta, L., Micela, G., Zinzi, A., Béjar, V.J.S., Biazzo, K., Bignamini, A., Bonavita, M., Borsa, F., del Burgo, C., Chauvin, G., Delorme, P., González Hernández, J.I., Gratton, R., Hagelberg, J., Janson, M., Langlois, M., Lanza, A.F., Lazzoni, C., Lodieu, N., Maggio, A., Mancini, L., Molinari, E., Molinaro, M., Murgas, F., Nardiello, D., 2023. The GAPS programme at TNG. XLVIII. The unusual formation history of V1298 Tau. *A&A* 679, A55. doi:10.1051/0004-6361/202244752.

Turri, D., Marzari, F., Polychroni, D., Testi, L., 2019. Dust-to-gas Ratio Resurgence in Circumstellar Disks Due to the Formation of Giant Planets: The Case of HD 163296. *ApJ* 877, 50. doi:10.3847/1538-4357/ab18f5, arXiv:1802.04361.

Turri, D., Miguel, Y., Zingales, T., Piccialli, A., Helled, R., Vazan, A., Oliva, F., Sindoni, G., Panić, O., Leconte, J., Min, M., Pirani, S., Selsis, F., Coudé du Foresto, V., Mura, A., Wolkenberg, P., 2018. The contribution of the ARIEL space mission to the study of planetary formation. *Experimental Astronomy* 46, 45–65. doi:10.1007/s10686-017-9570-1, arXiv:1804.06179.

Turri, D., Nelson, R.P., Barbieri, M., 2015. The role of planetary formation and evolution in shaping the composition of exoplanetary atmospheres. *Experimental Astronomy* 40, 501–522. doi:10.1007/s10686-014-9401-6, arXiv:1401.5119.

Turri, D., Schisano, E., Fonte, S., Molinari, S., Politi, R., Fedele, D., Panić, O., Kama, M., Changeat, Q., Tinetti, G., 2021. Tracing the Formation History of Giant Planets in Protoplanetary Disks with Carbon, Oxygen, Nitrogen, and Sulfur. *ApJ* 909, 40. doi:10.3847/1538-4357/abd6e5, arXiv:2012.14315.

Turri, D., Svetsov, V., 2014. The Formation of Jupiter, the Jovian Early Bombardment and the Delivery of Water to the Asteroid Belt: The Case of (4) Vesta. *Life* 4, 4–34. doi:10.3390/life4010004, arXiv:1401.7490.

Ward, W.R., 1981. Solar nebula dispersal and the stability of the planetary system I. Scanning secular resonance theory. *Icarus* 47, 234–264. doi:10.1016/0019-1035(81)90169-X.

Weidenschilling, S.J., 1977. Aerodynamics of solid bodies in the solar nebula. *MNRAS* 180, 57–70. doi:10.1093/mnras/180.2.57.

Weidenschilling, S.J., Davis, D.R., Marzari, F., 2001. Very early collisional evolution in the asteroid belt. *Earth, Planets and Space* 53, 1093–1097. doi:10.1186/BF03351708.

Weidenschilling, S.J., Marzari, F., Hood, L.L., 1998. The Origin of Chondrules at Jovian Resonances. *Science* 279, 681. doi:10.1126/science.279.5351.681.

Wisdom, J., Holman, M., 1991. Symplectic maps for the N-body problem. *AJ* 102, 1528–1538. doi:10.1086/115978.

Zhang, K., Gladman, B.J., 2022. GLISSE: A GPU-optimized planetary system integrator with application to orbital stability calculations. *New A* 90, 101659. doi:10.1016/j.newast.2021.101659.

Zhu, W., Dong, S., 2021. Exoplanet Statistics and Theoretical Implications. *ARA&A* 59, 291–336. doi:10.1146/annurev-astro-112420-020055, arXiv:2103.02127.